Guided Wave Tomography Based on Full Waveform Inversion

Rao, Jing; Ratassepp, Madis; Fan, Zheng

2016

Guided Wave Tomography Based on Full Waveform Inversion

Manuscript

J. Rao, M. Ratassepp, Z. Fan

School of Mechanical & Aerospace Engineering

Nanyang Technological University

50 Nanyang Avenue, Singapore 639798

February 26, 2016

Abstract

In this paper, a guided wave tomography method based on Full Waveform Inversion (FWI) is developed for accurate and high resolution reconstruction of the remaining wall thickness in isotropic plates. The forward model is computed in the frequency domain by solving a full-wave equation in a two-dimensional acoustic model, accounting for higher order effects such as diffractions and multiple scattering. Both numerical simulations and experiments were carried out to obtain the signals of a dispersive guided mode propagating through defects. The inversion was based on local optimization of a waveform misfit function between modeled and measured data, and was applied iteratively to discrete frequency components from low to high frequencies. The resulting wave velocity maps were then converted to thickness maps by the dispersion characteristics of selected guided modes. The results suggest that the FWI method is capable to reconstruct the thickness map of a irregularly shaped defect accurately on a 10 mm thick plate with the thickness error within 0.5 mm.

1 Introduction

Corrosion of pressure vessels, storage tanks and pipelines is a significant problem in petrochemical and nuclear industries [1, 2]. Detecting and quantifying the wall thickness loss due to the corrosion damage is of growing interest. Conventional ultrasonic thickness-gauging methods are tedious and expensive, especially for inaccessible areas [3]. Guided wave tomography offers good potential to estimate the remanent thicknesses of corrosion patches without accessing all points on the surface [4, 5, 6]. It uses the dispersion characteristics of guided waves, and reconstructs the thickness map by the inversion of ultrasonic signals captured by a transducer array around the inspection area. Research work has been carried out to develop guided wave tomography algorithms, including traveltime tomography [7, 8], diffraction tomography [5, 9], and hybrid algorithms which combine the previous two methods [10].

Traveltime tomography uses the arrival time of guided wave packets to reconstruct the slowness (reciprocal of velocity) distribution based on a ray model. Both straight [11] and bent [12] rays have been investigated in the guided wave tomography. However, by ignoring diffraction, this model is only valid when the defects are much larger than the wavelength of the guided wave, and the resolution of this method is limited by the width of the first Fresnel zone $\sqrt{L\lambda}$, where L is the distance between the source and the receiver and λ is the wavelength of the illuminating wavefield [13].

Diffraction tomography takes diffraction and scattering into account under a linearized scattering model such as the Born or Rytov approximations. Belanger *et al.* [5] investigated simple defects under the Born approximation, which relied on weakly scattering objects. The Rytov approximation, on the other hand, requires the phase of the total field and the incident field to be unwrapped [6], thus is only suitable for low contrast scatterings with little

2

noise. Theoretically diffraction tomography can improve the resolution to $\lambda/2$. However, it only works with small or low contrast defects where the phase shift travelling through the defect is small.

More recently, Huthwaite *et al.* [10] combined the bent ray tomography and the diffraction tomography and proposed a new HARBUT algorithm. This was initially developed for medical applications and it was then applied in guided wave tomography using its iterative version [14], and it can achieve the same resolution as the diffraction tomography.

In this paper, we introduce a full waveform inversion (FWI) method in the guided wave tomography for corrosion mapping. Such method was first developed in geophysics for seismic wave imaging [15, 16, 17]. It uses a numerical forward model to predict the scattering of guided wave through corrosion defects, and an iterative inverse model to reconstruct the corrosion profile. At each iteration, numerical modeling is performed with the aim of the least-squared minimization of the misfit between the modeled and the observed data. This approach overcomes the limitation imposed by ignoring crucial low frequency effects in traveltime tomography. Compared with other tomography methods which are limited by linear scattering, FWI allows higher order diffraction and scattering to be considered in its numerical solver, thus it is possible to capture more of the guided wave scattering physics which could lead to more accurate inversion results.

The Finite Difference (FD) method is usually applied in FWI as forward solver because it is faster and consumes less memory compared with the Finite Element (FE) method. It can be performed in both time and frequency domain. In our work, the calculation is performed only in the frequency domain, by considering the computational efficiency, as problems with multiple sources are easier to be solved [18]. Moreover, the multiscale strategy can mitigate the nonlinearity of the inverse problem through moving from

low to high frequencies, and therefore more likely to obtain the global optimization [19, 20]. Finally, the dispersion and the attenuation can be easily incorporated into the frequency domain with complex velocities [21, 22].

The structure of the paper is organized as follows. The theory of FWI based on the finite-difference frequency-domain method is presented in Section 2, including the forward modeling as well as the inversion method. Section 3 introduces the numerical simulations based on a simplified acoustic model using FD method and a more realistic elastic model using FE method. The choice of frequencies and the calibration method are also introduced in this section. Experimental setup and data processing are presented in Section 4. The performance of FWI including the sensitivity is discussed in Section 5 by two representative examples. The discussion of the multiscale inversion and computational aspects is followed in Section 6. Conclusions are summarized in the final section.

2 Theory

2.1 Forward modeling in the space-frequency domain

The frequency-domain two-dimensional acoustic wave equation in a constant density media can be written as

$$(\nabla^2 + K^2)p(x, y, \omega) = -s(x, y, \omega), \tag{1}$$

where $p(x, y, \omega)$ is the pressure (or displacement) wavefield, $s(x, y, \omega)$ being the source, ω being the angular frequency and $K(x, y, \omega) = \omega/v(\omega)$ is the wavenumber linked with the phase velocity v.

Equation 1 is discretized with the FD method using the mixed-grid approach [23, 24, 25]. Repeating this method at all grid points leads to a

4

large system of linear equations. In order to solve these equations, they are rewritten in the matrix form

$$AP = S \quad or \quad P = A^{-1}S, \tag{2}$$

where the complex-valued impedance matrix, also the forward modeling operator, is given by $A = \nabla^2 + K^2$, which is dependent on the frequency and physical properties of the medium. We now introduce 2D discretization. The pressure wavefield is computed at $l = n_x \times n_y$ grid points on the 2D regular grid, where n_x and n_y represent the number of grids in the horizontal and the vertical direction, respectively. The pressure wavefield P and the source term S at one frequency are mapped into $l \times 1$ column vectors, and the complex-valued impedance matrix A is a $l \times l$ matrix.

Equation 2 is often solved by the direct method of LU factorization. After LU decomposition of the matrix A, the factored A matrix can be reused to solve the forward problem for other source vectors, so that the multiple sources problem can be efficiently computed. This plays an essential role in the iterative solution of the inverse problem, because the forward solutions for real and "virtual" sources (explained later) are needed at each iteration. Equation 2 can be given as

$$LU[P_1 P_2 \cdots P_n] = [S_1 S_2 \cdots S_n], \tag{3}$$

where n is the number of the sources.

The absorbing boundaries along the edges of the model can be utilized to avoid the reflections from the edges [25, 26, 27], which allows the reduction of the model size.

2.2 Inverse problem in the space-frequency domain

Figure 1 outlines the structure of the FWI algorithm. The multi-resolution nature of the reconstruction is controlled by loop 1 over several discrete frequencies starting from low and moving towards higher frequencies. At each frequency several iterations are performed, corresponding to loop 2. At the end of each iteration at a given frequency, a new model parameter is calculated and is reset as the starting model for the next iteration until a predefined maximum iteration number is reached. This number is chosen between 20 to 40 in our studies. At each iteration, the residual data (difference between computed results from the current model and the observed data from experiments) is minimized in the sense of least squares. The velocity map obtained from the last iteration of the current frequency becomes the initial model for the next frequency. This process is repeated until the convergence criterion is reached at the highest frequency. The convergence criterion will be discussed in details in Section 3.4. The aim of the inversion is to create a set of model parameters m which can reproduce the observations by using the forward modeling. Such model parameters consist of the values of the squared slowness [19]. The theory of the FWI has been introduced in details in seismology [22, 28, 29], thus only principle equations are given here.

The weighted least squares norm of the objective function, i.e. the L_2 norm of the data residuals, is defined as

$$C^{(k)}(\mathrm{m}) = \frac{1}{2}\Delta \mathrm{d}^\dagger \mathrm{W}_d \Delta \mathrm{d}, \tag{4}$$

where $\Delta \mathrm{d} = d_{calc}^{(k)} - d_{obs}$ is the data residual (the difference between data $d_{calc}^{(k)}$ computed in the current model $\mathrm{m}^{(k)}$ and the observed data d_{obs}). The superscript $\dagger$ represents the transposed conjugate. W_d is a weighting vector that is used in the data residual to scale the relative contribution of each

6

component in the inversion, and k is the iteration number.

The inverse problem is to minimize the objective function, and it can be computed by using the gradient

$$G^{(k)} = Re\{J^t W_d \Delta d^*\}, \qquad (5)$$

where J^t is the transpose of the Fréchet derivative matrix (i.e. Jacobian matrix, $J = \frac{\partial P}{\partial m}$). Δd^* is the conjugate of the data residual and Re is the real part of a complex number.

Furthermore, in order to derive the expression for any of partial derivatives $\frac{\partial P}{\partial m}$ in equation 5, we take the partial derivatives of both sides of the forward equation 2 with respect to the ith model parameter m_i

$$A \frac{\partial P}{\partial m_i} = -\frac{\partial A}{\partial m_i} P. \qquad (6)$$

A "virtual" source term $f^{(i)} = -\frac{\partial A}{\partial m_i} P$ can be introduced as

$$\frac{\partial P}{\partial m_i} = A^{-1} f^{(i)}. \qquad (7)$$

An analogy between equation 2 and equation 7 indicates that partial derivatives $\frac{\partial P}{\partial m}$ are the solutions of a new forward model of the "virtual" source $f^{(i)}$. Thus, the link between the gradient vector (including the partial derivatives, $\frac{\partial P}{\partial m}$) and a new forward modeling can be established.

Since we can generate an equation similar to equation 7 for any value of i, all of the partial derivatives by the matrix equation can be given by

$$J = \left[\frac{\partial P}{\partial m_1} \frac{\partial P}{\partial m_2} \cdots \frac{\partial P}{\partial m_q} \right] = A^{-1} [f^{(1)} f^{(2)} \cdots f^{(q)}], \qquad (8)$$

where q is the number of model parameters, $q \leq l$. The computation of the elements of J requires to solve q forward-propagation problems using virtual

7

sources.

Thus, in order to obtain the gradient using equation 5, it is not necessary to compute the elements of partial derivatives J directly. Substituting equation 8 and $f^{(i)}$ into equation 5, it is obtained

$$G^{(k)} = Re \left\{ -\mathrm{P}^t \left[\frac{\partial \mathrm{A}^t}{\partial \mathrm{m}_i} \right] \mathrm{A}^{-1t} \mathrm{W}_d \Delta \mathrm{d}^* \right\}. \tag{9}$$

Since A^{-1} is symmetric in the acoustic problem, i.e. $[\mathrm{A}^{-1}]^t = \mathrm{A}^{-1}$, equation 9 can be given by

$$G^{(k)} = Re \left\{ -\mathrm{P}^t \left[\frac{\partial \mathrm{A}^t}{\partial \mathrm{m}_i} \right] \mathrm{A}^{-1} \mathrm{W}_d \Delta \mathrm{d}^* \right\}, \tag{10}$$

where $\mathrm{A}^{-1} \mathrm{W}_d \Delta \mathrm{d}^*$ is defined as backward propagated wavefield. The matrix $\frac{\partial \mathrm{A}^t}{\partial \mathrm{m}_i}$ can be easily computed by using the coefficients of the matrix A. Based on the reciprocity principle, the gradient is computed by zero-lag convolution of the forward-modeled wavefield P with the backward-propagated residual wavefield $\mathrm{A}^{-1} \mathrm{W}_d \Delta \mathrm{d}^*$. It means that only two forward models per source are required. The first forward problem is to obtain the wavefield P for a source position. The second forward problem calculates the backward propagated residual wavefield using a "composite" source formed by assembling data residuals.

In order to provide stable and reliable results, we apply some scaling and regularization to the gradient equation 10. It can be modified to

$$G^{(k)} = (diag\mathrm{H}_a + \epsilon I)^{-1} \mathcal{G}_{2D} Re \left\{ -\mathrm{P}^t \left[\frac{\partial \mathrm{A}^t}{\partial \mathrm{m}_i} \right] \mathrm{A}^{-1} \mathrm{W}_d \Delta \mathrm{d}^* \right\}, \tag{11}$$

where $diag\mathrm{H}_a = diag Re\{\mathrm{J}^t \mathrm{W}_d \Delta \mathrm{J}^*\}$ indicates the diagonal elements of weighted approximate Hessian H_a; ϵ denotes the damping factor and $\mathcal{G}_{2D}$ is the spatial smoothing operator.

The diagonal of the approximate Hessian H_a provides the proper preconditioner for the gradient which scales the tomographic model. The diagonal element of H_a is the scalar product of two partial derivative wavefields. Furthermore, as the scatterers are removed from the source location, the amplitudes of the partial derivative wavefields and the corresponding elements of H_a will decrease. Dividing data residuals by these squared amplitude terms is equivalent to remove the effect of geometrical amplitudes decreasing of partial derivative wavefields from data residuals. The damping factor ϵ is added to the diagonal elements of approximate Hessian, which can stabilize the inversion process because the H_a may be ill conditioned or singular. The smoothing operator $\mathcal{G}_{2D}$ is in the form of a 2D Gaussian spatial filter in this paper and its correlation length is adapted to inverted frequency components.

Finally, the model parameter vector is updated iteratively according to

$$m^{(k+1)} = m^{(k)} - \alpha^{(k)} g^{(k)} \tag{12}$$

where α is a scalar step length and g indicates the search direction of the objective function. In this paper, the inverse problem is solved by an iterative linearized approach using steepest-descent algorithm, which means that the direction of the gradient is the search direction $g^{(k)} = -G^{(k)}$. Moreover, the step length can be determined to minimize the objective function along the search direction [30].

3   Numerical modeling

3.1   Elastic model based on FE method

FE simulations are performed on a 10 mm aluminum plate (Young's modulus= 70.8 GPa, Poisson's ratio= 0.33, and density= 2700 kg/m^3) with the

size of $1100{\times}1100$ mm^2. Cubic shape eight node elements with the size of 1 mm are used in the mesh which ensures that more than 30 elements per wavelength at the highest frequency is exploited for accurate modeling [31]. The corrosion patches with desired shapes are modeled by removing the elements from the mesh. The plate is surrounded by absorbing region to avoid reflections coming from the edges [32]. The waves are monitored by a circular array with a diameter of 700 mm consisting of 64 nodes acting as transducers as shown in Figure 2(a). Out-of-plane displacement is applied in one of the nodes and the wavefields are measured by the other 63 nodes. This is repeated for all the source-receive combinations resulting in a $64{\times}63$ signal matrix. The source excitation used in simulations is a 5 cycle Hann windowed toneburst signal at a central frequency of 50 kHz, which has around 15 dB bandwidth from 35 to 65 kHz. By applying the normal force at this frequency it ensures that nearly pure A_0 mode is generated [33]. Also, around this frequency the A_0 mode is highly dispersive and therefore sensitive to thickness variations, as shown in Figure 2(b). More details about the mode selection for guided wave tomography have been discussed by Huthwaite [34].

3.2   Acoustic model based on FD method

FD simulations are performed in a two-dimensional space domain neglecting thickness of the plate which is an approximation to the full plate model but it is capable to model any guided modes with dispersive properties [14]. It needs to be noted that mode conversions do not occur in the acoustic model. This is consistent with the 3D FE model, as the thickness variation of corrosion-like defects are relatively smooth, thus causing less mode conversions than sharp discontinuities [35]. Plate with the same dimension as in FE models is meshed by grid points with 2 mm spacing. This guarantees the calculation accuracy which requires at least 4 grid points per shortest wavelength [25].

The plate is surrounded by absorbing areas with the same width as in FE models. Omni-directional pressure waves are excited and monitored with the similar array configuration as described in the FE setup.

3.3 Data processing

As the inversion algorithm is based on the FD acoustic modeling, the input scattered signals from the FE elastic modeling should be calibrated to account for possible deviations between the two models. One way to reduce the amount of phase and amplitude errors of the input is to match the wave propagation results of the two homogeneous models (without scatterers) by introducing the calibration factor defined as [14]

$$Q = \frac{fft^*(B_{FD})}{fft^*(B_{FE})} \tag{13}$$

where fft represents the fast Fourier transform, $*$ being the complex conjugate, and B_{FD} and B_{FE} are the data from receivers in homogeneous models by FD and FE methods, respectively.

Additionally, the Gaussian filter is used to smooth the background before subsequent iterations. The aim of this filter is to minimize the effects of artifacts from each iteration. The selection for correlation length of the Gaussian filter is around $\lambda/2$.

After the inversion the reconstructed velocity map from FD and FE models are converted to thickness maps by the known dispersion relationship between the thickness, frequency and the phase velocity.

3.4 Frequency selection and convergence

The iteration over sequential frequencies enables the inversion to start from a homogeneous velocity model and moving towards the desired high-resolution

true velocity model. At each frequency the iterated model should provide the updated model with a close neighborhood to the global minimum for the next frequency. Global minima can be found more easily at lower frequencies where the velocity model resembles to the homogeneous background model [36]. However, the well-defined strategy for selecting appropriate frequencies in waveform tomography has not yet been established [37]. Here we propose the largest frequency step between the frequency iterations according to the wavenumber k distribution of the scattered wave field from the diffraction tomography [38]. The scattered field contains the transmission part which is limited within a circle of radius $\sqrt{2}k_1$ in the K space and the reflection subset which is contained between $\sqrt{2}k_1$ and $2k_1$. Transmission wavenumbers at the lower frequency f_1 are always included in the larger wavenumber subset at the frequency f_2 within the circle of radius $\sqrt{2}k_2$. In order to account for all the reflection wavenumbers in the inversion, the relationship between two subsequent modelings at wavenumbers k_1 and k_2 should satisfy the relation $k_2 \leq \sqrt{2}k_1$. Thus for the inversion based on non-dispersive waves the relationship between the frequencies is directly $f_2 \leq \sqrt{2}f_1$. This is slightly a stricter criterion for the current study as the wave propagation is dispersive and the growing rate of wavenumber in frequency is slower than non-dispersive waves.

The convergence of the results over iterations is examined by comparing the average relative thickness change E around the thinnest area with respect to the nominal thickness, similarly as in [14],

$$E_j^{(i)} = \frac{\overline{|T_j^{(i)}(x,y) - T_j^{(i-1)}(x,y)|}}{T_0},\qquad(14)$$

where $T_j^{(i)}(x,y)$ is the thickness at position (x,y) for the current iteration i at jth frequency component, and T_0 is the nominal thickness. The value of

$E \leq 10^{-2}$ is accurate for the thickness estimation in engineering applications. However, the threshold for stopping the inversion is set to be $E \leq 0.5 \times 10^{-3}$ which is a stricter limit due to the slow conversion rate of the FWI algorithm. It should be noted that at lower frequencies a fixed number of iterations are performed and the value E is approaching the convergence, while the above convergence criterion is only checked at the highest frequency. There are possibilities to optimize the choice of the frequencies and the number of iterations, but this is beyond the scope of the current study.

4 Experiments

The experimental setup is shown in Figure 3(a). Experimental measurements were performed on two 1100mm×1100mm×10mm aluminum plates. A flat-bottomed circular hole with a wall boundary having an angle of 30° to the plate surface was machined in the first plate. Its diameter on the plate surface is 60 mm and its depth is 50% of the thickness. The second plate contains a irregularly shaped defect with the maximum depth of 5 mm, which was produced by a computer numerical control (CNC) milling machine, and defect was constructed by removing the material layer by layer. A zoomed picture of the defect is shown in Figure 3(b).

The measurement was carried out on a 700 mm diameter circle around the defect, with 64 generator/monitor positions equally spaced along the circle. The A_0 guided mode was generated by a PZT transducer (Panametrics V1011) at one position, and measured at other positions by a Polytec OFV-505 laser vibrometer. In each measurement, a 5 cycle Hann windowed toneburst signal at 50 kHz was generated by a Tiepie Handyscope HS3. Figure 3(c) shows a typical signal measured by the vibrometer. A gating function similar to [14] was applied to remove unwanted components and obtain the first arrival wavepacket. To avoid the reflection from the edge, only trans-

mitted signals were used and thus the measurements were taken on half of the circle with 33 signals measured, as shown in Figure 3(a). This process was repeated 64 times to build up a matrix of 64×33 signals.

Similarly as in the simulations, the measured signals need to be calibrated using Equation 13 before they can be used for inversion. However in the experiment, due to the presence of the defect, signals in a homogeneous medium can only be obtained from limited positions. Therefore, we only measured the waveform in one of the receiver position (shown in Figure 3(a)), which was not affected by the scatterer, and mapped it to all other receivers according to their positions. This was a reasonable approach, given that the anisotropy in sound speed is limited in this plate.

5 Reconstruction results

5.1 Single regular defect

The first modeling was performed with a circular defect situated in the center of a 64 element circular array, as shown in Figure 4(a). The defect is a flat-bottomed circular hole with a stepped wall boundary. It has the surface diameter of 60 mm($\simeq 1.3\lambda$ at 35 kHz, 1.9λ at 60 kHz) and its thickness reduction is 50%.

Figure 4(b), (c) and (d) show the monochromatic reconstruction of the thickness at 35 kHz obtained after 40 iterations for the FD model, the FE model and the experiment, respectively. Figure 4(e), (f) and (g) show the polychromatic reconstruction of the plate thickness at 60 kHz. Sequential frequency group with frequencies 35, 46 and 60 kHz was used according to the frequency selection criterion discussed in Section 3.4. Homogeneous background was used as the starting model at the lowest frequency and 20 iterations at each frequency. The velocity map obtained in the final iteration

14

at each frequency was used as a starting model for the next frequency. The work was carried out on a HP Z820 work station with 32-core and 128G memory. Each forward model in the FD simulation took about 25 seconds to solve, while the inversion took around 1.5 hours to reach the convergence.

It can be seen from the figures that the defect was reconstructed in all cases, with sharper images at higher frequencies. Very clear images were obtained from the acoustic modeling. Some artifacts at the location of an array can be seen in the images from elastic models but they do not degrade the quality of the interior of the resolvable area. This is due to the under-sampling of the wavefield in the circular array. According to Simonetti *et al.* [39], the minimum number of transducers in a circular array to correctly sample a wavefield can be expressed as

$$N > \frac{4\pi r}{\lambda}, \tag{15}$$

where r is the radius of the image to be free from grating lobes. At 60 kHz ($\lambda = 34$ mm), 130 transducers would be needed to correctly reconstruct the image for an area of 700 mm in diameter. However, it is not practical to have too many transducers in the experiment, particularly for field applications, and therefore the number of transducers is limited to 64 in our studies with expected reduction in the imaging area that is free from grating lobes. Another possible reason for the artifact at the position of the array could be the inability to cancel entirely the source contribution in the models during the inversion which arise from the singularities in Green's function and its near-field effects [21]. Notable artifacts are observed in the images reconstructed from the experimental data. Despite the reason of the undersampling as discussed above, the excited wavefields may not be ideally omni-directional which means that the phase and amplitude of the signal may vary with respect to the excitation angle. As in the calibration, the signals without the

scatterer are generated synthetically, and therefore this mismatch between the true and synthesized signal leads to the phase and amplitude errors in the inversion. In addition, the results can be affected by the noise, the measurement positioning error, the length of the gating function, and the slight anisotropy of the material [40].

Comparisons between the reconstructions and the original thickness profile across the defect extracted from Figure 4(b)-(g) are shown in Figure 5. It can be seen that in both FD and FE cases the hole's depth is reconstructed already at 35 kHz. The reconstruction from experimental data slightly underestimates the depth by 0.4 mm. The reconstruction of all cases at 60 kHz slightly overestimates the depth but the largest error obtained by experimental data is 0.3 mm from the true value. The thickness reconstruction from the experiment by using only the transmission part (a matrix of 64×33 signals) is similar to the simulation results based on both reflection and transmission parts (a matrix of 64×63 signals). These results clearly demonstrate that the resolution compared to the resolution of traveltime tomography, i.e. $\sqrt{L\lambda}=$ 153 mm (at 60 kHz) is improved significantly.

It is worth mentioning that an attempt was made to carry out the inversion directly at 60 kHz from a homogeneous velocity model but the convergence was not achieved indicating that the starting model was not accurate enough for the inversion. The reason is that at the lower frequency, the initial estimate is obtained at the longer scale component, which has slow varying features and fewer minima [36]. Therefore, the neighborhood of the global minimum is more likely to be captured at such scale.

5.2   Irregularly shaped defect

The reconstruction of the irregularly shaped defect as in the experiment was carried out in Figure 6(a). The depth of the defect varies irregularly up to 5

mm and its largest extent is around 220 mm. The defect is characterized by complicated shape and smooth variations in thickness. Three sequential frequencies 35, 46 and 60 kHz were used for the inversion, and at each frequency 30 iterations were applied. The forward model in this case took 50 seconds to solve, slightly longer than the previous case due to the complication in the velocity map. The inversion process took around 4.5 hours to get the results shown in Figure 6(b), (c) and (d).

It can be seen that the original shape with fine details of the defect is reconstructed very well from the acoustic model. The reconstruction based on the elastic model can also accurately capture almost all details of the defect. The image from the experimental data is more noisy due to the reasons explained previously. However, the overall shape of the defect and thinnest parts match the original image very well.

The cross-sections of Figure 6 with the largest corrosion depths are shown in Figure 7(a) and (b). It can be seen that the profiles of the defect are very accurately reconstructed by using the data from the acoustic model. The reconstructions using the data from the elastic model and the experiment are also very good although the deepest points in the defect are slightly underestimated, with an error of about 0.5 mm. It is worth noting that the reconstruction results between the experimental data and the elastic model using FE simulations are very close to each other, suggesting that the inversion can be reliably performed with only the transmitted signals. This is also observed by other researchers in the previous work [5].

6   Discussion

The results presented in this paper for two different defects have shown that the FWI is a useful tool to obtain high resolution thickness mapping for plate-like structures by using only transmission measurement of the total

field. The results of the irregular defect also indicate that the resolution of FWI is slightly compromised when defects were reconstructed from the elastic model and experimental data compared to the equivalent reconstruction using the simplified acoustic model. The reason comes from the fact that two-dimensional FD model is an approximation for the realistic three-dimensional wave propagation model and can yield some restrictions in the inversion if the modeling data severely deviate from each other. This has been shown by Huthwaite [6] where the scattering from small scatterers of the two models within the Born approximation was compared. It was found that the scattered waves from two-dimensional acoustic and three-dimensional elastic models behave similarly only in a limited scattering region in the transmission zone.

One of the benefits of FWI lies in its multiple frequency strategy that helps to process data subsets of increasing resolution to incorporate smaller wavenumbers in the tomographic models. The inversion can be started from the homogeneous background model at low frequency where the global minimum can be more easily found as the velocity errors in the waveforms remain below a half-cycle [21]. As mentioned before, traveltime tomography provides accurate reconstructions when the size of the object to be imaged is much larger than the wavelength λ and the width of the first Fresnel zone $\sqrt{L\lambda}$. For the diffraction tomography to be valid the phase shift travelling through the defect must be small. The FWI is an alternative approach to fill the gap between traveltime tomography and diffraction tomography. The reconstruction results of the irregular defect demonstrated that the inversion is successful even when the defect is larger than the first Fresnel zone and its smaller details around the size of the wavelength can be determined.

Compared with existing methods, the major limitation of the FWI approach is its computational complexity and cost. The relationship between

the measurement data and the model is nonlinear and the inversion needs to be iterated several times before it converges. The calculation results showed that the convergence for a single frequency can be obtained in 20 to 40 iterations. Depending on the total number of frequencies needed for the inversion, much more iterations would be required. Although the current computational cost is acceptable as an off-line imaging method, it is possible to improve the time efficiency of the FWI. In this work the conventional steepest descent algorithm was used for numerical optimization. The convergence rate could be improved significantly if more advanced optimization methods, such as quasi-Newton algorithm [41], are used. Another solution for reducing iterations is to use a low resolution tomography algorithm to build a more accurate starting model that will subsequently be refined by FWI. Finally, the sequential execution used to solve the equations of the forward problem in this work can be replaced by the massively parallel solver MUMPS algorithm [42], which distributes the solving processes over the processors and improves the calculation speed by more than one order.

7 Conclusions

In this paper, the full waveform inversion (FWI) method is developed for guided wave tomography on plate-like structures. It includes a forward solver to predict the scattering measurements in a two-dimensional acoustic model and an inverse model to update the velocity map iteratively, which is then linked to the thickness map via the dispersion relations of selected guided wave modes. The algorithm uses multiple frequency strategy, which applies the image produced at lower frequency as the initial model for the higher frequency. Consequently, the reconstruction of the thickness map is less dependent on the initial model, while keeps high resolution to small features.

In this work, a simple circular hole and a complex shaped defect were used

for the demonstration of the algorithm via both numerical simulations and experiments. It was shown that the minimum thickness could be estimated to be within 0.5 mm for a 10 mm thick plate. The FWI method allows higher order scattering effects to be considered in the model, thus could lead to improved resolution compared with other guided wave tomography methods, and the details will be investigated in the future work.

8   Acknowledgements

References

[1] A. Groysman, Corrosion for everybody, Springer, New York, 2010.

[2] C. L. Willey, F. Simonetti, P. B. Nagy, G. Instanes, Guided wave tomography of pipes with high-order helical modes, NDT & E. Int. 65 (2014) 8–21.

[3] J. Krautkramer, H. Krautkramer, Ultrasonic Testing of Materials, Springer, Berlin, 1969.

[4] X. Zhao, R. L. Royer, S. E. Owens, J. L. Rose, Ultrasonic lamb wave tomography in structural health monitoring, Smart Mater. Struct. 20 (10) (2011) 105002.

[5] P. Belanger, P. Cawley, F. Simonetti, Guided wave diffraction tomography within the born approximation, IEEE Trans. Ultrason. Ferroelectr. Freq. Control 57 (6) (2010) 1405–1418.

[6] P. Huthwaite, Evaluation of inversion approaches for guided wave thickness mapping, Proc. R. Soc. A. 470 (2014) 20140063.

[7] J. McKeon, M. Hinders, Parallel projection and crosshole lamb wave contact scanning tomography, J. Acoust. Soc. Am. 106 (5) (1999) 2568–2577.

[8] M. Malyarenko, M. Hinders, Fan beam and double crosshole lamb wave tomography for mapping flaws in aging aircraft structures, J. Acoust. Soc. Am. 108 (4) (2000) 1631–1639.

[9] E. V. Malyarenko, M. K. Hinders, Ultrasonic lamb wave diffraction tomography, Ultrasonics 39 (4) (2001) 269–281.

[10] P. Huthwaite, F. Simonetti, High-resolution imaging without iteration: a fast and robust method for breast ultrasound tomography, J. Acoust. Soc. Am. 130 (3) (2011) 1721–1734.

[11] K. R. Leonard, M. K. Hinders, Multimode lamb wave tomography with arrival time sorting, J. Acoust. Soc. Am. 117 (4) (2005) 2028–2038.

[12] A. Volker, J. Bloom, Experimental results of guided wave travel time tomography, Rev. Prog. Quant. Nondestruct. Eval. 30 (2011) 215–222.

[13] P. R. Williamson, A guide to the limits of resolution imposed by scattering in ray tomography, Geophysics 56 (2) (1991) 202–207.

[14] P. Huthwaite, F. Simonetti, High-resolution guided wave tomography, Wave Motion 50 (5) (2013) 979–993.

[15] A. Tarantola, A strategy for nonlinear elastic inversion of seismic reflection data, Geophysics 51 (10) (1986) 1893–1903.

[16] R. G. Pratt, M. H. Worthington, Inverse theory applied to multisource cross-hole tomography. part 1: acoustic wave-equation method, Geophys. Prosp. 38 (1990) 287–310.

[17] J. Virieux, S. Opertor, An overview of full-waveform inversion in exploration geophysics, Geophysics 74 (6) (2009) WCC1–WCC26.

[18] K. J. Marfurt, Accuracy of finite-difference and finite-element modeling of the scalar and elastic wave-equations, Geophysics 49 (5) (1984) 533–549.

[19] L. Sirgue, R. G. Pratt, Efficient waveform inversion and imaging: A strategy for selecting temporal frequencies, Geophysics 69 (1) (2004) 231–248.

[20] S. Operto, J. Virieux, J. X. Dessa, G. Pascal, Crustal seismic imaging from multifold ocean bottom seismometer data by frequency domain full waveform tomography: Application to the eastern nankai trough, J. Geophys. Res. 111 (2006) doi:10.1029/2005JB003835.

[21] R. G. Pratt, Seismic waveform inversion in the frequency domain, part 1: Theory and verification in a physical scale model, Geophysics 64 (3) (1999) 888–901.

[22] R. G. Pratt, C. Shin, G. J. Hicks, Gauss-newton and full newton methods in frequency-space seismic waveform inversion, Geophys. J. Int. 133 (1998) 341–362.

[23] C. H. Jo, C. Shin, J. H. Suh, An optimal 9-point, finite-difference, frequency-space 2-d scalar extrapolator, Geophysics 61 (2) (1996) 529–537.

[24] I. Stekl, R. G. Pratt, Accurate viscoelastic modeling by frequency-domain finite differences using rotated operators, Geophysics 63 (5) (1998) 1779–1794.

[25] B. Hustedt, S. Operto, J. Virieux, Mixed-grid and staggered-grid finite-difference methods for frequency-domain acoustic wave modelling, Geophys. J. Int. 157 (2004) 1269–1296.

[26] J. P. Berenger, A perfectly matched layer for absorption of electromagnetic waves, J. Comput. Phys. 114 (1994) 185–200.

[27] R. Clayton, B. Engquist, Absorbing boundary conditions for acoustic and elastic wave equations, Bull. Seism. Soc. Am. 67 (6) (1977) 1529–1540.

[28] C. Shin, K. Yoon, K. J. Marfurt, K. Park, Efficient calculation of a partial derivative wavefield using reciprocity for seismic imaging and inversion, Geophysics 66 (6) (2001) 1856–1863.

[29] C. Ravaut, S. Operto, L. Improta, J. Virieux, Multiscale imaging of complex structures from multifold wide-aperture seismic data by frequency-domain full-waveform tomography: Application to a thrust belt, Geophys. J. Int. 159 (2004) 1032–1056.

[30] D. Vigh, E. W. Starr, J. Kapoor, Developing earth model with full waveform inversion, The Leading Edge 28 (2009) 432–435.

[31] P. Huthwaite, F. Simonetti, M. J. S. Lowe, On the convergence of finite element scattering simulations, Rev. Prog. Quant. Nondestruct Eval. 29 (2010) 65–72.

[32] M. Castaings, C. Bacon, Finite element modeling of torsional wave modes along pipes with absorbing materials, J. Acoust. Soc. Am. 119 (6) (2006) 3741–3751.

[33] P. Belanger, P. Cawley, Lamb wave tomography to evaluate the maximum depth of corrosion patches, Rev. Prog. Quant. Nondestruct Eval. 27 (2008) 1290–1297.

[34] P. Huthwaite, R. Ribichini, P. Cawley, M. J. S. Lowe, Mode selection for corrosion detection in pipes and vessels via guided wave tomography, IEEE Trans. Ultrason. Ferroelectr. Freq. Control 60 (6) (2013) 1165–1177.

[35] Y. Cho, Estimation of ultrasonic guided wave mode conversion in a plate with thickness variation, IEEE Trans. Ultrason. Ferroelectr. Freq. Control 47 (3) (2000) 591–603.

[36] C. Bunks, F. M. Saleck, S. Zaleski, G. Chavent, Multiscale seismic waveform inversion, Geophysics 60 (5) (1995) 1457–1473.

[37] E. M. T. Takougang, A. J. Calvert, Application of waveform tomography to marine seismic reflection data from the queen charlotte basin of western canada, Geophysics 76 (2) (2011) B55–B70.

[38] F. Simonetti, L. Huang, N. Duric, P. Littrup, Diffraction and coherence in breast ultrasound tomography: A study with toroidal array, Med. Phys. 36 (7) (2009) 2955–2965.

[39] F. Simonetti, L. Huang, N. Duric, On the spatial sampling of wave fields with circular ring apertures, Journal of Applied Physics 101 (8) (2007) 083103.

[40] P. Belanger, Feasibility of thickness mapping using ultrasonic guided waves, Ph.D. thesis, Imperial College, London (2009).

[41] R. Brossier, S. Operto, J. Virieux, Seismic imaging of the complex on shore structures by 2d elastic frequency-domain full-waveform inversion, Geophysics 74 (6) (2009) WCC105–WCC118.

[42] P. R. Amestoy, A. Guermouche, J. Y. L'Excellent, S. Pralet, Hybrid-scheduling for the parallel solution of linear systems, Parallel Comput. 32 (2006) 136–156.
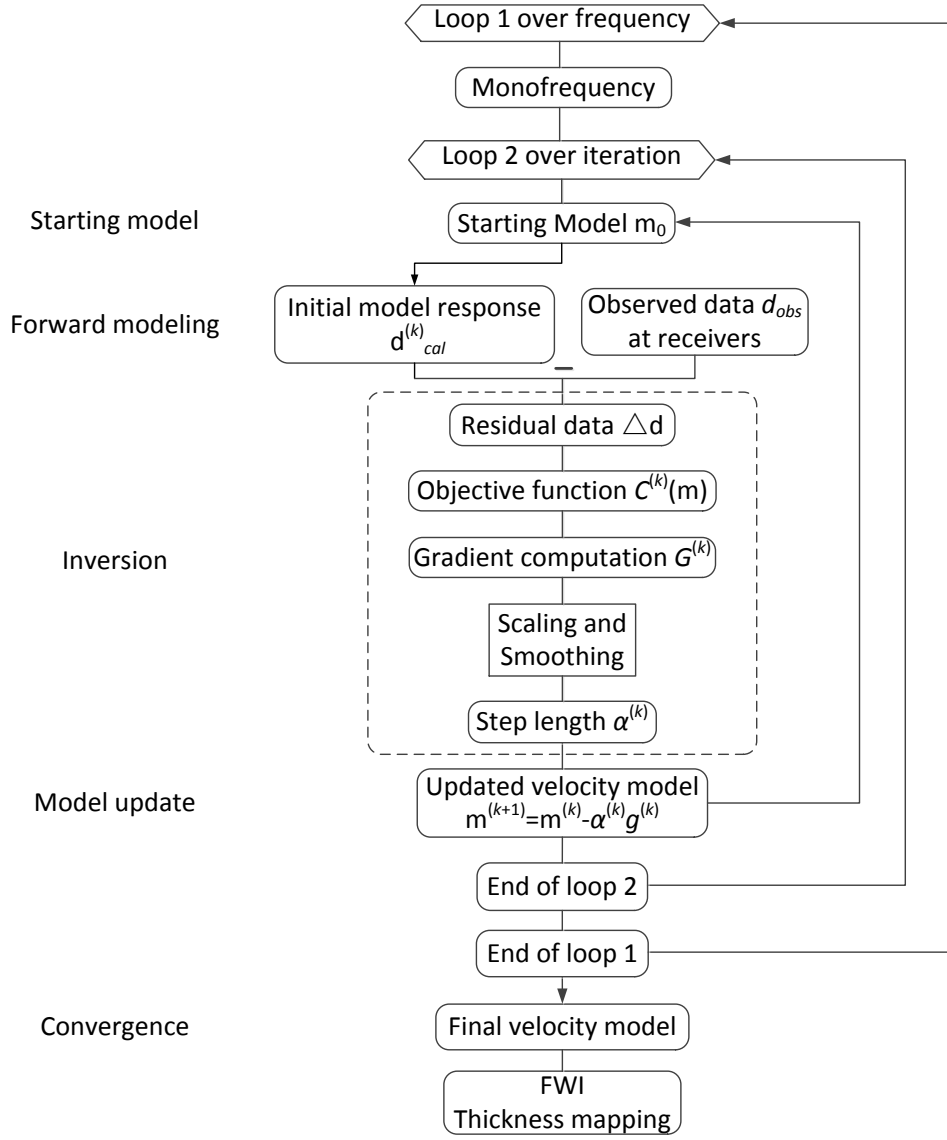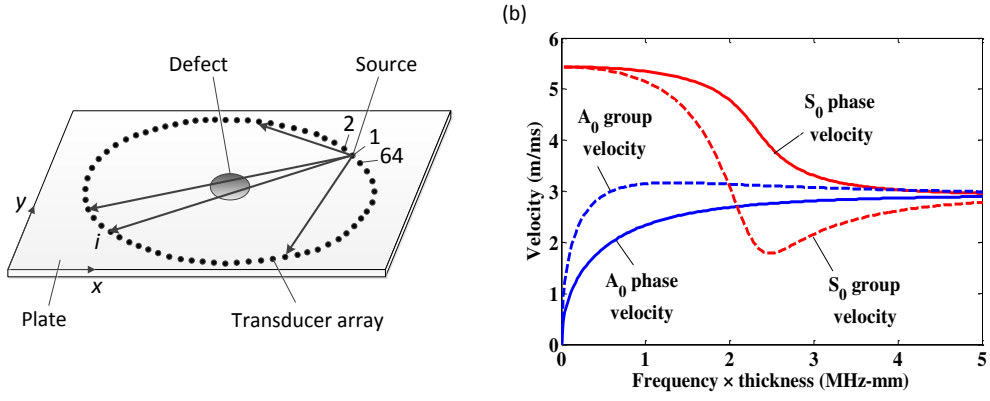
Figure 1: Structure of the FWI algorithm.

Figure 2: (a) The configuration of a circular transducers array for guided wave tomography on a plate. (b) Dispersion curves of Lamb wave in a 10 mm aluminum plate.
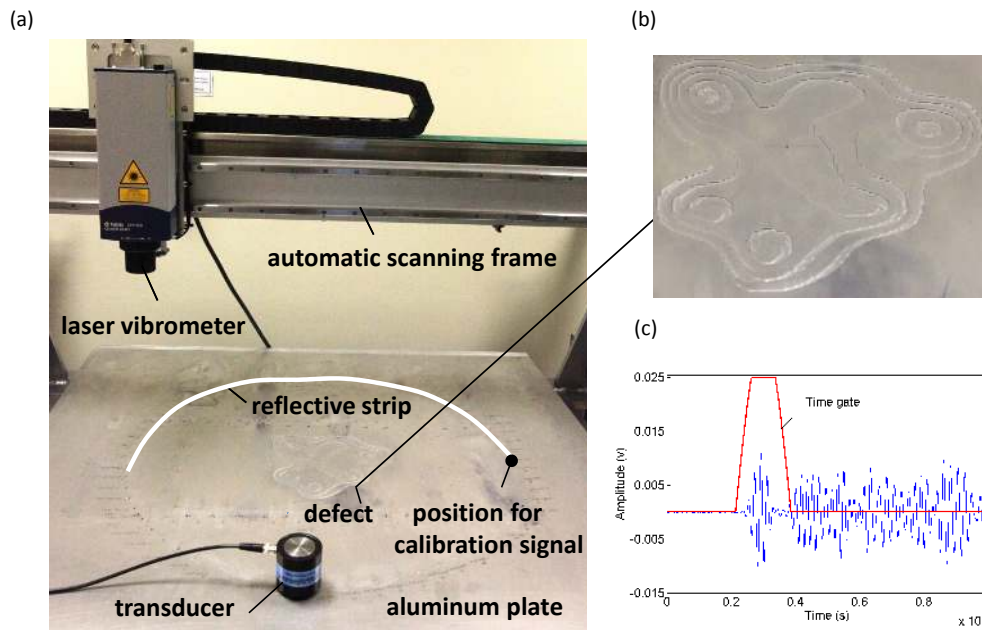
27

Figure 3: (a) Experimental setup with the irregularly shaped defect; (b) a zoomed picture of the defect; (c) typical time-trace from the experiment with chosen time window.
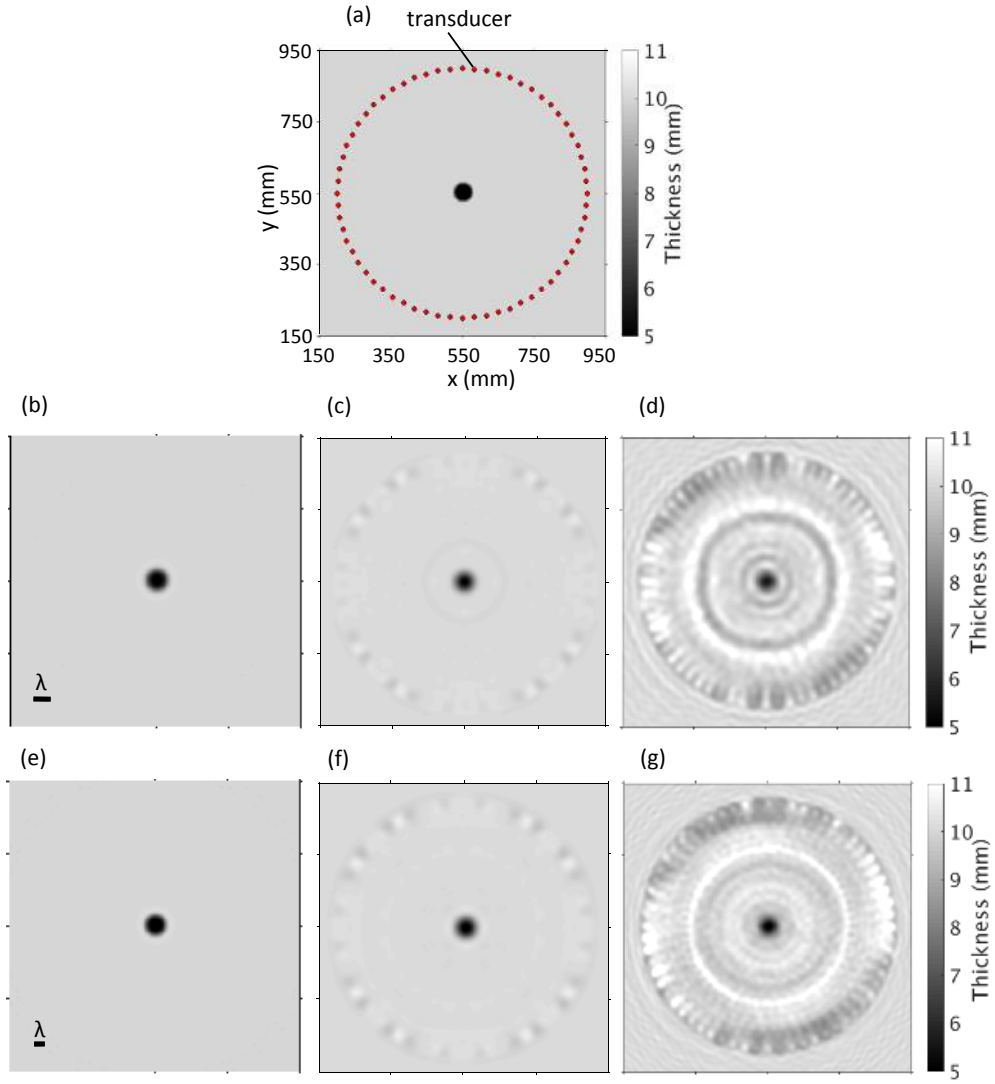
Figure 4: FWI reconstructions with a single central defect. Original model (a); monochromatic 35 kHz in the acoustic model (b), the elastic model (c), the experimental data (d); polychromatic 60 kHz in the acoustic model (e), the elastic model (f), and the experimental data (g).
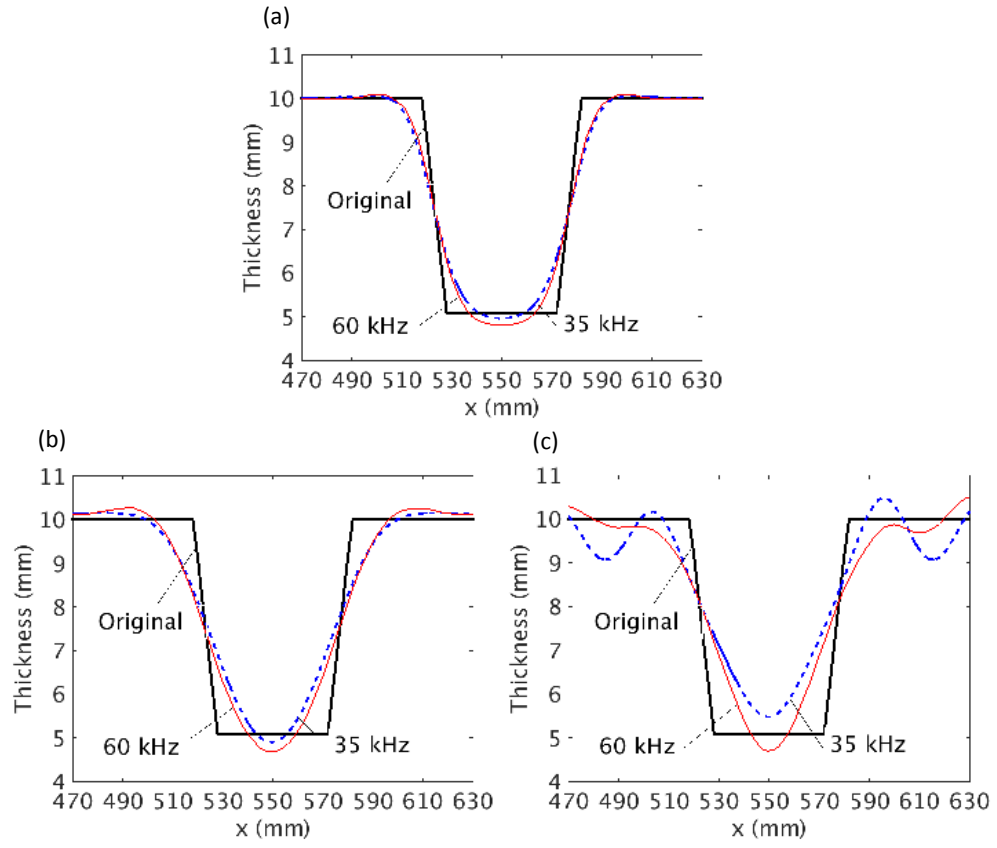
Figure 5: Cross sections of the thickness reconstructions of a single central defect along the central line in the acoustic model (a), the elastic model (b), and the experimental data (c).
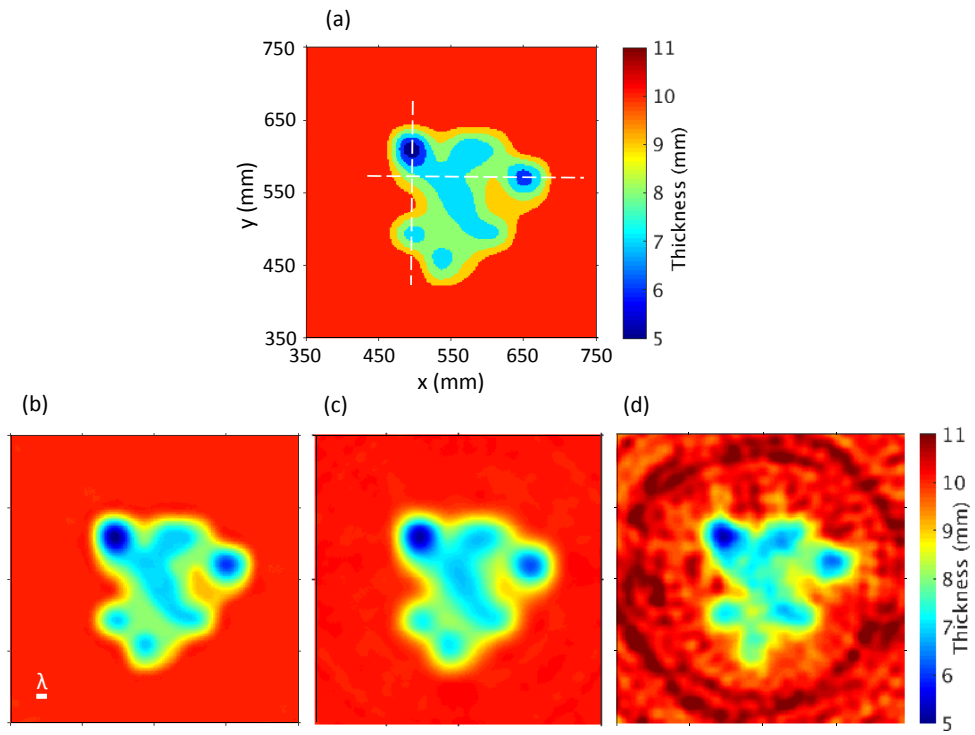
Figure 6: Polychromatic FWI reconstructions applied to the irregular defect at 60 kHz. Original model (a), the acoustic model (b), the elastic model (c), and the experimental data (d).
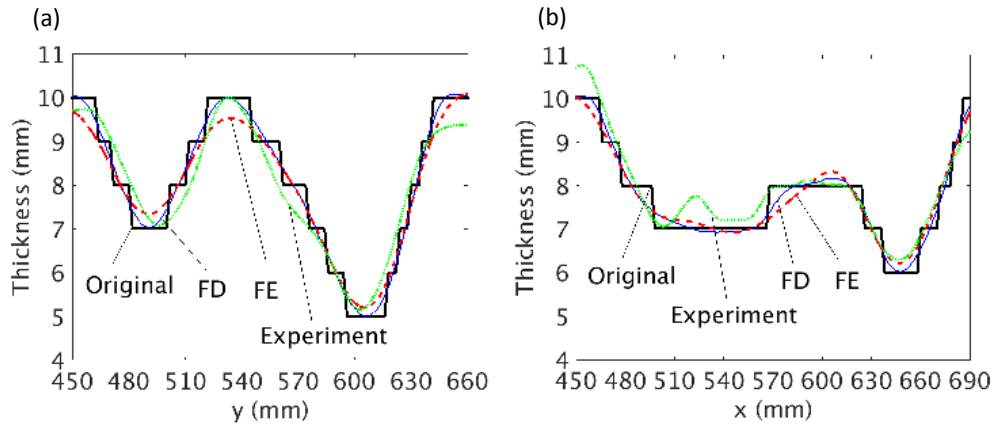
Figure 7: Cross sections of reconstructions of the irregular defect along the line marked in Figure 6a along the vertical line (a) and the horizontal line (b).